Editors' Suggestion

Dispersion and deformation of molecular patterns written in turbulent air

Willem van de Water [1,*], Nico Dam [2,3] and Enrico Calzavarini [4]

[1] *Laboratory for Aero and Hydrodynamics, Delft University of Technology and J.M. Burgers Centre for Fluid Dynamics, 2628 CD Delft, The Netherlands*

[2] *Institute for Molecules and Materials, Radboud University, 6500 GL Nijmegen, The Netherlands*

[3] *Mechanical Engineering Department, Eindhoven University of Technology, P.O. Box 513, 5600 MB Eindhoven, The Netherlands*

[4] *Université de Lille, ULR 7512–Unité de Mécanique de Lille Joseph Boussinesq (UML), F-59000 Lille, France*

(Received 23 May 2023; accepted 2 November 2023; published 12 January 2024)

Molecular tagging is used to study the dispersion and deformation of patterns written in turbulent air. The writing is done by fusing O_2 and N_2 molecules into NO in the focus of a strong ultraviolet laser beam. By crossing several of these laser beams, patterns that have both small and large scales can be painted. The patterns are visualized a while later by inducing fluorescence of the NO molecules with a second UV laser and registering the image. The width of the lines that make the pattern is approximately 50 μm, a few times the Kolmogorov length η, the smallest length scale in turbulence, while the largest size of the patterns (≈4 mm) is inside the inertial range of the used turbulent jet flow. At small scales molecular clouds disperse under the joint action of molecular diffusion and turbulence. The experiments reveal this highly nontrivial interaction. At inertial-range scales (≈200 η) we verify the Batchelor dispersion of objects whose size is inside the inertial range. Patterns are compressible objects and spontaneously develop concentration fluctuations. We show for the first time the nontrivial statistical properties of these fluctuations. Finally, we use the information in written and deformed lines to quantify turbulent intermittency, obtaining results that agree with the established scaling anomaly of velocity structure functions.

DOI: 10.1103/PhysRevFluids.9.014502

I. INTRODUCTION

In molecular tagging the molecules of the flow are used as flow tracers [1,2]. Tagging is accomplished by exciting available molecules to a metastable state [3] using laser excitation, or by creating new molecules that are not part of the base flow [4,5]. The initial pattern of tagged molecules is shaped by focusing the writing laser in lines, or in more complicated structures. Reading—seeing how the pattern has evolved—is done by observing phosphorescence or laser-induced fluorescence.

In this paper we will discuss the application of molecular tagging to a turbulent flow of air at Taylor-scale Reynolds numbers $R_\lambda = \mathcal{O}(500)$. We will argue that molecular tagging is well suited to study small-scale turbulent mixing of gases, perhaps even better than it is suited to measure the velocity field.

The length and timescales of turbulence define the context of molecular tagging. Turbulent motion is characterized by a range of spatial scales which goes from the largest stirred scale to the smallest one, the Kolmogorov scale η where the scale-to-scale energy flux ϵ is dissipated by molecular viscosity ν. The intermediate scales are called the inertial range, characterized by an

*Corresponding author: w.vandewater@tudelft.nl

algebraic scale dependence of turbulence statistics. At the Reynolds numbers cited, the smallest length scales are $\mathcal{O}(10\,\mu\text{m})$ and the smallest timescales are $\mathcal{O}(10\,\mu\text{s})$, which sets the minimum lifetime of tagged molecules.

In this paper we study turbulent mixing and velocimetry through the dispersion of small clouds of NO molecules in air. The writing is done by weakly focusing UV laser beams with a wavelength of 193 nm in a turbulent air flow emerging from a jet, and fusing the O_2 and N_2 molecules into the long-lived molecular tracer NO [4]. Tracer molecules are made visible by exciting them with a second laser and observing the UV fluorescence using an intensified camera [6].

This is one of a few techniques (coined APART in Ref. [4]) for molecular tagging in a flow of a gas which have been explored in the past few years. We will now provide a brief review; more extended reviews of molecular tagging velocimetry (MTV), also in flows of liquids, can be found in Refs. [1,2,7]. In our research we have been inspired by the RELIEF technique [3], where oxygen molecules are tagged by exciting them to a metastable vibrational state by means of a ns pulsed laser. Reading is done by inducing fluorescence with UV light a while ($\approx$10 μs) later. Other techniques include hydroxyl tagging, where OH is made by photodissociation of water vapor [8], or the creation of ozone molecules by photodissociating O_2 [8], followed by the [slow $\mathcal{O}(20\,\mu\text{s})$] recombination to O_3. The addition of (toxic) NO_2 molecules allows one to create NO tracers by photodissociation, coined VENOM in Ref. [9]. With femtosecond laser electronic excitation N_2 can be dissociated, which is followed by recombination and emission of visible light during $\mathcal{O}(10\mu\text{s})$. This velocimetry scheme has been named FLEET [5]. Finally we mention tagging of added biacetyl molecules, which decay by slow phosphoresence [10,11]. It turns out that in biacetyl tagging the spatial resolution is compromised by collisional quenching [11]. To the best of our knowledge, only two molecular tagging techniques have been used to obtain quantitative turbulence data that can be compared to the result of more conventional techniques [6,12]. However, a great promise of MTV techniques is their application in harsh environments, such as combustion, or in flows that cannot be seeded.

For gases, mass diffusion approximately equals the diffusion of momentum; their ratio, the Schmidt number, $\nu/D_{\text{mol}} \approx 1$. Specifically, for our experiment, NO in air, $\text{Sc} = 0.62$. This implies that mass diffuses in a time interval over which the smallest vortices in turbulence remain coherent. It imposes a fundamental constraint on turbulent velocimetry of motion on the smallest length and timescales: they will remain uresolved.

In the context of dispersion of a passive substance, a fundamental question is how molecular diffusion and turbulence interact. Specifically, will the joint action of turbulence and molecular diffusion be just additive, or will the result be less or more than the sum? In a seminal paper Saffman [13] concluded that the spreading of a cloud with respect to its center of mass is more than the sum, while the dispersion of the center of mass itself is less than the sum. The point is that the Lagrangian trajectories of the Brownian particles of the diffusing substance do not coincide anymore with the trajectories of fluid parcels. This question is most acute in gases where $\text{Sc} = \mathcal{O}(1)$, which befits the present paper.

Early experiments by Townsend [14,15] on the dispersion of heat spots in decaying turbulence appeared to support his analysis, but a sign error was noted in Ref. [13]. The dispersion of heat is characterized by the Prandtl number, in air $\text{Pr} = 0.72$, which is comparable to the Schmidt number of molecular substances. The shape and decay of thermal wakes was measured in an Eulerian frame, and compared to exact solutions of the convection-diffusion equation in regions of constant shear. The comparison to the experimental results showed that the size of these regions extends to 15 η, suggesting that the turbulent velocity field is smooth on scales much larger than the Kolmogorov scale η [14]. However, intermittency should lead to smaller length scales which are relevant for high-order statistics [16].

Experiments by Mickelsen [17] in grid turbulence on the dispersion of light (He) and heavy molecules (CO_2) with widely different diffusivities concluded that there is no interaction effect: in these experiments turbulent dispersion and molecular diffusion were found to be independent and simply additive.

Mazzino and Vergassola [18] found that the manner in which molecular diffusion interacts with turbulent dispersion is determined by the Lagrangian velocity autocorrelation function. This was demonstrated using a model calculation involving a synthetic velocity field. If $D_{\rm tot}$ is the total dispersion rate of a diffusing substance in turbulence, then the difference $D_{\rm tot} - D_{\rm mol}$ could be made both to increase or decrease with increasing $D_{\rm mol}$, with the understanding that $D_{\rm mol}$ is a substance property, and $D_{\rm tot}$ also embodies the properties of the flow.

The dispersion of point clouds in a turbulent channel flow was studied numerically by Kontomaris and Hanratty [19] where molecular diffusion was modeled using a stochastic process. In this inhomogeneous flow, both a diffusive enhancement or depletion of the convective contribution to dispersion was found, depending on the spatial direction chosen. Because the turbulent velocity field is incompressible, next to expanding, also contracting regions exist and a blob of passive tracer material develops a filamentary structure. This affects the contribution of molecular diffusion, which will be more rapid in regions of steep gradients. Several exact solutions embodying these phenomena are discussed in Ref. [20]. Similarly, for *laminar* shear flow, the interaction with molecular diffusion—Taylor dispersion [21] was analyzed in several geophysically inspired flow models by Ref. [22].

The subject of the interaction between turbulence and molecular diffusion is not without controversy. Taylor states that the dispersion of a passive scalar is determined by the motion of fluid parcels only, independent of the molecular diffusivity [23]. More specifically, Pope [24] states that the probability of the local scalar concentration $C(\boldsymbol{x}, t)$, conditioned on the velocity $\boldsymbol{u}(\boldsymbol{x}, t)$, is independent of the molecular diffusivity $D_{\rm mol}$ in the limit of infinite Reynolds number. However, while this may hold for global averages, and modeling of scalar transport, small-size structures—the subject of this paper—will still spread due to molecular diffusion.

The organization of this paper is as follows. In Sec. II we describe models for the widening of written lines. The experimental setup and image analysis is discussed in Sec. III. Results on the dispersion of lines and dots are shown in Sec. IV. Written lines are stretched, folded and compressed by turbulence and develop large concentration fluctuations. The statistical properties of these fluctuations are discussed in Sec. IV E. Finally we discuss the measurement of velocity structure functions and their anomalous scaling in Sec. V. A brief account of the results already appeared in Ref. [25]. The present paper describes the details of the experimental methods and expands on the results, further extending them to include large-scale concentration fluctuations and velocimetry.

II. TURBULENCE AND MOLECULAR DIFFUSION

In case of purely diffusive spreading the linear size $\sigma(t)$ of a Gaussian cloud with one-dimensional concentration profile $C(x, t) \propto \exp[-x^2/\sigma^2(t)]$ that starts from a point grows in time as $\widetilde{\sigma}^2(\tilde{t}) = \frac{4}{\rm Sc}\tilde{t}$, where the size of the cloud was made dimensionless with the Kolmogorov length η, $\widetilde{\sigma} = \sigma/\eta$, and time t was made dimensionless with the Kolmogorov time τ_η, $\tilde{t} = t/\tau_\eta$. The question now is how this simple form is changed in the presence of turbulence.

Saffman [13] showed that the interaction between turbulence and molecular diffusion is subtle: the dispersion of a tracer cloud relative to its point of release is *less* than the sum of turbulent dispersion and diffusion. The argument is that molecules forget their history more quickly than fluid parcels. However, the dispersion of clouds around their center of mass is *more* than the sum of turbulent dispersion and molecular diffusion. The constructive interaction results in an extra contribution which is third-order in time,

$$\widetilde{\sigma}^2(\tilde{t}) = \frac{4}{\rm Sc}\left(\tilde{t} + \frac{1}{9}\tilde{t}^3\right). \tag{1}$$

The prefactor $1/9$ is consistent with the assumption of homogeneous isotropic turbulence. The $\tilde{t}^3$ dependence was already concluded by Townsend [15], but with a prefactor tailored to the case of decaying turbulence. It must be noted that all previous experiments [14,15,17] involved spreading

of a substance or heat from a fixed source. This is not the context of Eq. (1), which only holds in the Lagrangian frame of turbulence.

The interaction term Eq. (1) was reproduced by the stochastic analysis of Sawford and Hunt [26] and Buaria *et al.* [27,28] who also allowed for the finite initial size $\sigma(0)$ of the cloud. This led them to the following expression for the growth of a molecular cloud in turbulence:

$$\widetilde{\sigma}^2(\tilde{t}) = \widetilde{\sigma}^2(0) + \underbrace{\widetilde{\sigma}^2(0)\left(\frac{\tilde{t}^2}{3} - \frac{7\,S_\epsilon}{18\sqrt{15}}\,\tilde{t}^3\right)}_{\text{a}} + \underbrace{\frac{4}{\mathrm{Sc}}\left(\tilde{t} + \frac{1}{9}\tilde{t}^3\right)}_{\text{b}}, \tag{2}$$

where S_ϵ is the dissipation skewness, $S_\epsilon \approx 0.5$ [29], and where term (a) expresses the influence of turbulence, while term (b) is the interaction between turbulence and diffusion of Eq. (1).[1]

In part (a) of Eq. (2) the growth of the cloud due to turbulence starts quadratically in time. In fact, the analysis of Buaria *et al.* [27] assumes for the contribution linear in time

$$2\langle \boldsymbol{r}(0)\cdot\mathbf{S}(0)\cdot\boldsymbol{r}(0)\rangle\, t = 0, \tag{3}$$

with the strain tensor $S_{ij} = (\partial u_i/\partial x_j + \partial u_j/\partial x_i)/2$, and where averages are over turbulence realizations and orientation $\boldsymbol{e}(0)$ of the initial pair separation, $\boldsymbol{r}(0) = r(0)\boldsymbol{e}(0)$. Equation (3) is justified when $\boldsymbol{e}(0)$ is uncorrelated with the rate-of-strain tensor $\mathbf{S}$, so that the average involves a factor $\langle\mathbf{S}\rangle$ which is zero in isotropic turbulence. As was argued by Dhariwal and Bragg [31], whether this assumption holds or not depends on the statistical state of the system. If, at $t = 0$, the particles are inserted in the flow randomly, e.g., as they would be in the numerical simulation of Ref. [27], then $\langle \boldsymbol{e}(0)\cdot\mathbf{S}(0)\cdot\boldsymbol{e}(0)\rangle = 0$. If, however, the particles have experienced the history of the flow, then their relative orientation $\boldsymbol{e}(0)$ should be correlated with the strain tensor $\mathbf{S}$. This more natural condition is the context of our experiment. It would be very hard to realize in a numerical simulation, as a prohibitive amount of particles must be traced to find two particles separated by $\lesssim \eta$ at initial time.

We conclude that the growth of a cloud due to turbulence in our experiment should involve a term linear in time, $2\,\widetilde{\sigma}^2(0)\,\tau_\eta\langle \boldsymbol{r}(0)\cdot\mathbf{S}(0)\cdot\boldsymbol{r}(0)\rangle\, t$. An upper limit of this term is reached when $\boldsymbol{e}(0)$ is directed along the eigenvector of $\mathbf{S}$ with the largest eigenvalue λ_1, which leads to the simple model,

$$\widetilde{\sigma}^2(t) = \widetilde{\sigma}^2(0)\big(1 + 2\,S\,\tilde{t}\big) + \frac{4}{\mathrm{Sc}}\left(\tilde{t} + \frac{1}{9}\tilde{t}^3\right), \tag{4}$$

with $S = \lambda_1\tau_\eta = 0.357$ [32].[2] The correlation between $\boldsymbol{e}(0)$ and $\mathbf{S}(0)$ will also affect the higher order terms in part (a) of Eq. (2), which will completely change the analysis of Ref. [27].

The linear approximation of Eq. (4) defines an effective diffusion coefficient D_{eff}, $\sigma^2(t) = \sigma^2(0) + 4D_{\mathrm{eff}}\,t$, with

$$D_{\mathrm{eff}} = D_{\mathrm{mol}} + \sigma^2(0)\,S/2\tau_\eta, \tag{5}$$

where D_{mol} is the molecular diffusion coefficient. The effective diffusion coefficient depends on the turbulence intensity through the Kolmogorov timescale τ_η; in quiescent flow, $\tau_\eta \to \infty$ and $D_{\mathrm{eff}} = D_{\mathrm{mol}}$.

The $\tilde{t}^3$ dependence in Eqs. (2) and (4) owes to the enhanced diffusion in regions of strain-Taylor dispersion- and should not be confused with Richardson's famous t^3 law [34]. This law was inferred

[1]Note that Eq. (2.17) in Ref. [27] is for the squared separation of molecular pairs, which is *twice* the squared cloud size [30]. However, the squared Gaussian width σ is *half* the squared cloud size. Also, Eq. (2.17) in Ref. [27] is for the particle separation in three dimensions whereas we consider one-dimensional Gaussian cross sections, which leads to a factor 3. In summary, there is a factor 3 between term b of Eq. (2) and the corresponding term in Eq. (2.17) of Ref. [27].

[2]This is close to the dimensional estimate $\tau_\eta\langle(\partial u/\partial y)^2\rangle = (2/15)^{1/2} = 0.365$ for homogeneous isotropic turbulence [31,33] which was used here and in our earlier paper [25].

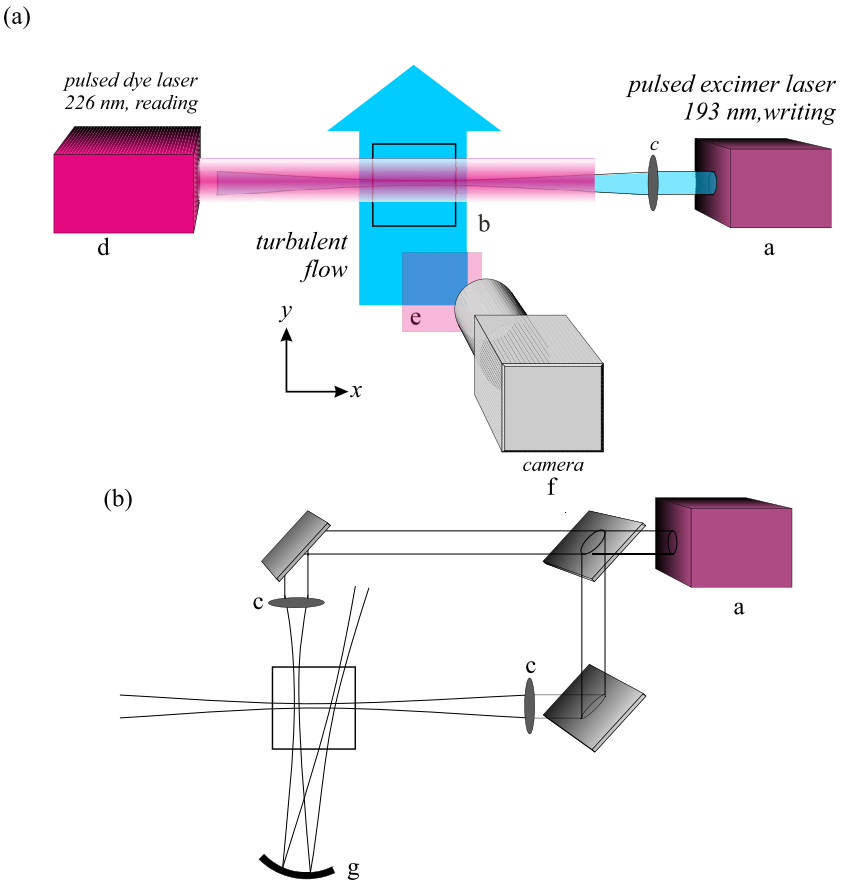

FIG. 1. Experimental setup for writing in air. (a) Writing single lines. The beam of an Ar-F excimer laser (a) at $\lambda = 193$ nm is focused into the 6.4×6.4 mm^2 field of view (b) by lenses (c). A while later the created NO molecules are illuminated by a light pulse from the dye laser (d) at $\lambda = 226$ nm using a broad beam that embraces the written pattern. This wavelength is blocked by an absorption filter (e) which transmits the induced fluorescence. The UV image is registered by a gated, intensified camera (f). The turbulent flow emanates from a jet; in the field of view the flow is approximately homogeneous and isotropic, with typical mean velocity $V = 45$ m/s, root-mean-square velocity $v = 12$ m/s, Taylor-scale Reynolds number $R_\lambda = 514$, Kolmogorov scale $\eta = 14$ μm, and Kolmogorov time $\tau_\eta = 13$ μs. (b) By crossing the writing beam several times with a secondary beam, using a lens and spherical mirror (g) to focus it, a double cross can be written.

from a rather daring analysis of experiments on the dispersion of clouds, volcano ash and balloons. It holds for times that are so long that the vortices in which the scalar started have lost coherence. In Sec. IV D we will argue that these times are out of reach in our experiment. For very long times, $t \gg \tau_\eta$, but with δx within the inertial range, $\delta x(t)$, will increase exponentially [31,33].

III. EXPERIMENT

We here describe the generation of a strongly turbulent jet flow, the optics to write and read patterns, and the processing of the fluorescence images.

Our experimental setup is sketched in Fig. 1. Two variants of this setup were used: with one writing laser beam we studied the widening of lines (initial width $\delta \approx 50$ μm $\approx 3.6\,\eta$) with three intersecting laser beams [as shown in Fig. 1(b)], and employing the nonlinearity of the writing

process [6] we define two dots whose separation $\Delta \approx 3.4$ mm lies in the inertial range ($\Delta \approx 200\,\eta$), while the dot size is comparable to the beam width δ. By measuring the width of lines $\sigma(t)$ and the separation of dots $\Delta(t)$, turbulent mixing both on small and large scales is studied in a frame that moves with the flow: the Lagrangian frame.

A. Turbulent flow

Strong turbulence in air was created in the efflux of a jet. At its orifice (with $d = 1$ cm diameter) the velocity is near sonic, but it slows down to a mean velocity $V = 40$ m/s at a distance $40\,d$ from the orifice where all measurements were done. The turbulence was characterized using hot-wire anemometry, using probes with a sensitive length of 200 μm and time response 50 μs. At the operating conditions the typical time and length scales of our experiment ($\tau_\eta = 15$ μs and $\eta = 15$ μm) are too small for a measurement of the turbulent dissipation rate ϵ using hot-wire anemometry. Therefore, the well-established scaling behavior of the turbulence properties of a jet was used to obtain the characteristics at the operating conditions from a measurement at much lower velocities.

In particular, the turbulent dissipation rate ϵ follows from the Kolmogorov relation

$$\epsilon = C_\epsilon \frac{v^3}{L}, \tag{6}$$

with L the integral length scale, and v the turbulent velocity. Assuming isotropy, ϵ was measured from a velocity signal $v(t)$ of the stationary probe,

$$\epsilon = 15\nu\langle(dv/dy)^2\rangle = 15\frac{\nu}{V^2}\langle(dv/dt)^2\rangle, \tag{7}$$

where we have used Taylor's frozen turbulence hypothesis. The time and space resolution of the hot-wire anemometer allowed measurement of ϵ up to $V = 8$ m/s. Taking the orifice diameter as the integral scale L, an effective $C_\epsilon = 0.47$ was determined, which compares well to that found in Ref. [35]. At the conditions of our tagging experiments, the finite width of the lines, $\sigma = 4\,\eta$ at the instant of writing, and the further widening of the lines due to turbulent dispersion and molecular diffusion ($\sigma = 6\,\eta$ at $t = \tau_\eta$) prevents direct measurement of ϵ from velocity gradients. However, the turbulent velocity v can be determined sufficiently accurately and can then be used together with Eq. (6) to find ϵ (and thus the turbulence length and timescales η and τ_η, respectively).

B. Writing and reading

Tracer NO molecules are formed in the waist region of a gently focused, tunable ArF excimer laser beam (Λ-Physik, various models).

Along this focus NO is formed over a length of approximately 1 cm. Therefore, the line extends outside the 6.4×6.4 mm^2 field of view of the camera. The tagged line has a waist diameter of about 50 μm. The duration of the writing laser pulse is ≈20 ns, which is instantaneous on the timescale of the turbulence. Using lenses and (spherical) mirrors, the main excimer beam can be crossed two times, resulting in a written pattern consisting of two crosses. The beam is refocused in each of the two crosses.

The reading laser is fired with delays ranging from 3 μs to as much as 35 μs with respect to the tagging laser. This frequency-mixed Nd:YAG-pumped dye laser is operated at a wavelength of 226 nm to visualize the created NO tagging molecules. The probe laser excites the γ bands of NO, and the resulting LIF emission from the excited (A) state is detected with the camera system. In the experiments the dye laser beam is aligned anticolinearly to the main excimer beam and both travel perpendicularly to the mean flow direction. The beam cross section was adjusted to result in maximal intensity while still encompassing the written line. Also the reading of the advected and deformed line is instantaneous on the timescale of the turbulence.

The UV fluorescence from the NO molecules is observed with an intensified gated CCD camera. The light incident on the camera is filtered using a high-pass filter that removes Rayleigh scattered light from both lasers while transmitting most of the NO fluorescence. The write-read delay t is controlled by timing the respective laser pulses using a multi-channel delay generator (Stanford DG535), which also synchronizes the camera gate to the read laser pulse. The 1024^2 pixel camera images are captured using a 12 bits frame grabber and then stored for off-line processing.

C. Image processing

The wrinkled lines of the deformed patterns are traced using an image processing technique based on active contours which finds their backbone $\boldsymbol{x}_i(s)$ [36]. Next, the profiles of perpendicular sections of instantaneous lines i are determined by fitting Gaussians to the line intensity I_i^l,

$$I_i^l(\zeta, s) = I_i(s)\, \mathrm{e}^{-\zeta^2/\sigma_i^2(s,t)}, \tag{8}$$

where ζ is measured perpendicular to the line center $\boldsymbol{x}_i(s)$, $\sigma_i(s,t)$ is the line width, s is the curvilinear coordinate, and t the time since writing.

Briefly, an active contour in an image is a line, endowed with physical properties (such as elasticity), which is evolved dynamically to find a best fit to the corresponding image object. Technically, this is done by turning the image into a potential energy surface with an energy minimum at the sought image object, i.e., the image of the fluorescing NO line [37,38].

In the sequel, all statistical properties of wrinkled lines involves this backbone. Its location $\boldsymbol{x}_i(s) = (x_i(s), y_i(s))$ has noise, which is mainly due to photon noise in the registered images. Further, the coordinates $(x_i(s), y_i(s))$ may suffer from errors made in tracing the line's backbone.

In addition to the position $\boldsymbol{x}_i(s)$ and Gaussian width $\sigma_i(s)$ of the lines, we will also be interested in the intensity $I_i(s)$ on their backbone, which provides information on the fluctuating scalar concentration on lines $\boldsymbol{x}_i$. A point of concern in our experiments is the illumination inhomogeneity of the laser beams. The writing laser beam is (weakly) focused with an intensity maximum in the center of the image. The reading laser beam, which is used to visualize the NO tracer distribution by inducing fluorescence, embraces the wrinkled lines, but the intensity in a beam cross section is not homogeneous. A map of these intensity variations on the x-y plane can be made by registering the intensity $I_i(s)$ at the line positions $\boldsymbol{x}_i(s)$ in a turbulent flow. These lines randomly sample an interval on the y axis. Due to the mean flow its location on the y axis shifts to larger values with increasing delay time while its size grows. The result of this experiment at delay times $t = 20$ μs and $t = 30$ μs is shown in Fig. 2, which demonstrates that at $t = 30$ μs the fluctuating lines have not yet reached the limits of the Gaussian reading beam.

The intensity variation along x is modeled by a quadratic fit, which was used to normalize the intensity of lines $I_i(s)$. No correction was made for the intensity profile of the reading beam cross section, as we only have information about its two-dimensional projection. The intensity of both writing and reading laser varies from shot to shot, that is from one line to the other. Therefore, the intensity of each line was normalized by the line-averaged intensity, $\tilde{I}_i(s) = I_i(s)/\langle I_i(s)\rangle_s$.

D. Turbulence characterization

A few typical images of lines are shown in Fig. 3. As the delay time between writing and reading increases, the lines become increasingly wrinkled. In Fig. 3 we show the variation of both mean and turbulent velocities across the field of view of the camera. These experiments were done at the highest jet back pressure. The relative variation of $v(x)$ is 2.5%, which illustrates the homogeneity of the turbulent velocity field over the field of view. In our experiments we use the measured $v(x)$ and Eq. (6), to infer the small-scale turbulence characteristics, η and τ_η as in Eqs. (6) and (7).

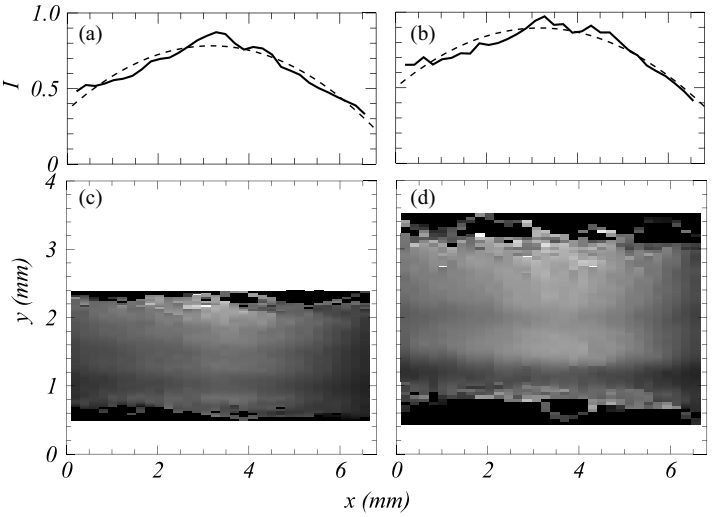

FIG. 2. Map of the laser intensity distribution made by 4×10^3 turbulent lines at two delay times between writing and reading (a, c) $t = 20$ μs, (b, d) $t = 30$ μs. The intensity variation depends on the fine tuning of the laser, which was different for the two delay times. (a, b) Full lines: mean profiles in x; dashed lines: quadratic function used in the normalization of the intensity profiles $I_i(s)$ of lines.

IV. RESULTS ON TRACER DISPERSION

We show results at very short times, where turbulent dispersion and molecular diffusion act additively and then discuss line widening at long times (up to $4\tau_\eta$) where the effects of the interaction

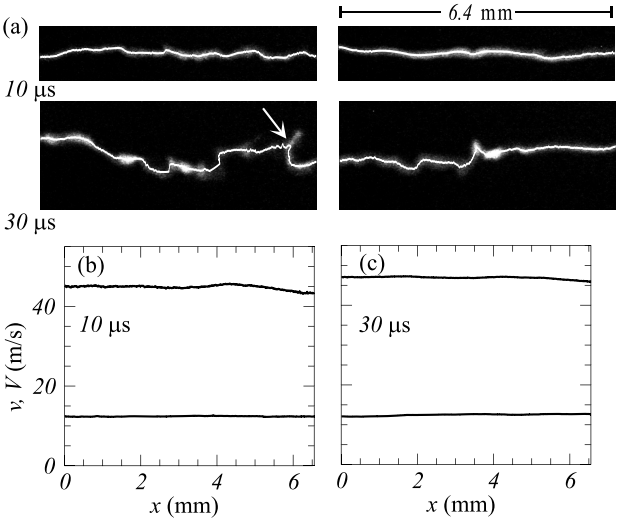

FIG. 3. (a) Written lines, seen at a delay of 10 μs (top) and 30 μs (bottom). The bright lines indicate the centroids (backbones) of the lines. They were determined from the images using the technique of active contours [36]. As can be seen at the largest time delay, these fits are not perfect. The arrow points to a loop that is missed. (b, c) Mean (upper lines) and rms velocity (lower lines) in the field of view of our camera. (b) At a time delay of $t = 10$ μs, (c) at $t = 30$ μs. At $t = 10$ μs, the turbulent velocity v varies from $v = 12.3 \ldots 12.6$ m/s across the image, while at $t = 30$ μs, $v = 12.1 \ldots 12.7$ m/s.

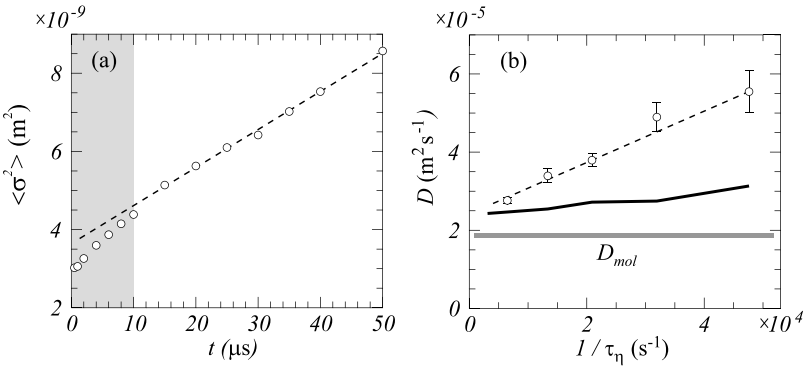

FIG. 4. (a) Diffusion coeffcient of NO in still air. Symbols are $\langle\sigma^2(t)\rangle$, dashed line is $\sigma^2(0) + 4\,D_{\rm mol}\,t$, with $D_{\rm mol} = 2.42 \times 10^{-5}$ m^{2}s^{-1}. At short times (gray area) the diffusion is anomalous due to the tagging process [6]. (b) Dots: experiment, $D_{\rm eff} = (\langle\sigma^2(t)\rangle - \langle\sigma^2(t_0)\rangle)/4\,(t - t_0)$ measured from the width of lines for a range of turbulent velocities u and times t ranging from $(t - t_0)/\tau_\eta = 0.1$ to $(t - t_0)/\tau_\eta = 0.5$. The initial time is $t_0 = 10$ μs, when diffusion has become normal. The error bars are the rms variation of $D_{\rm eff}$ along the written line. Dashed line: model Eq. (5); solid line: using Eq. (2). The gray line indicates the molecular diffusion coefficient.

between turbulence and diffusion play a role. We next focus on dots, instead of lines, and study their growth with time. By separating two dots over an inertial range distance at initial time, we retrieve Batchelor dispersion, which should also be influenced by the interaction effect.

A. Effective diffusion

At short times, the Gaussian width of lines grows diffusively, $\sigma^2(t) = \sigma^2(0) + 4\,D_{\rm eff}t$, where in the absence of turbulence $D_{\rm eff} = D_{\rm mol}$. In the first 10 μs after the writing laser pulse, Fig. 4(a) shows that diffusion is anomalous due to the heat released in writing; after that time we find $D_{\rm mol} = 2.42 \times 10^{-5}$ m^{2}s^{-1}, which is larger than the literature value, $D_{\rm mol} = 1.99 \times 10^{-5}$ m^2 s^{-1} [39]. Both the anomaly at short times, and the elevated value of $D_{\rm mol}$ are related to the tagging process [6]. We measure $D_{\rm eff}$ from the growth of the line width from $(t - t_0)/\tau_\eta = 0.1$ to $(t - t_0)/\tau_\eta = 0.5$,

$$D_{\rm eff} = \frac{\left\langle\sigma_i^2(t)\right\rangle_i - \left\langle\sigma_i^2(t_0)\right\rangle_i}{4\,(t - t_0)}. \tag{9}$$

The initial time is $t_0 = 10$ μs, when diffusion has become normal.

We varied the turbulent velocity u, and thus the Kolmogorov time τ_η by varying the mean flow velocity of the jet, as explained in Sec. III A. Averages $\langle\ \ \rangle_i$ were done over $\approx 10^3$ independent lines i, and over the central 2 mm of the lines, where the width is constant.

We compare the experimental result, shown in Fig. 4, to the model Eq. (5), and to the finite difference computed from Eq. (2). At these small times, $t \ll \tau_\eta$, the influence of the interaction term is negligible. The effective diffusion $D_{\rm eff}$ in Eq. (5) depends on the initial squared width of the line: the measured $\sigma(0)$ is 6.0 ± 0.1 μm. The simple model agrees well with the data, while there is a large discrepancy with the prediction of Eq. (2). As explained in Sec. II the context of our experiment, where tracers are indigenous to the flow, differs from the context of the analysis in Buaria *et al.* [27] where particles are inserted at will. Consequently, a term linear in t is missing in part (a) of Eq. (2), which causes the discrepancy with the experiment.

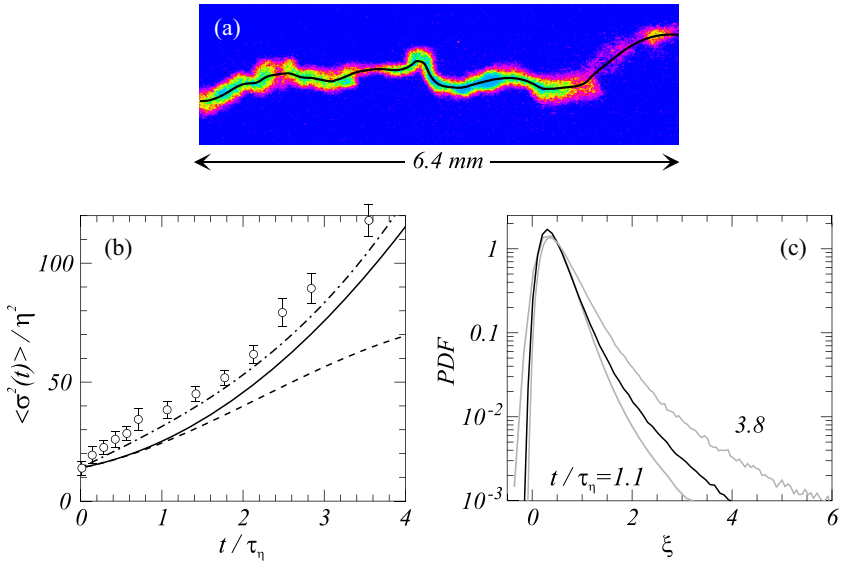

FIG. 5. The widening of lines written in a strongly turbulent flow is due to both molecular diffusion and turbulent dispersion. (a) The line has been registered a time $t = 35$ μs after it was written. It is shown together with a fit $\boldsymbol{x}(s)$ of its backbone; these fits were made using the technique of active contours [36]. The line profile was fitted by Gaussians $I^l(\zeta, s) = I(s)\exp(-\zeta^2/\sigma(s)^2)$ where ζ is measured perpendicular to the line backbone, which determined their width $\sigma(s)$, where s is the curvilinear coordinate. At each time delay the average of $\sigma^2(s,t)$ was done over 4×10^3 independent lines and over each individual line. (b) Symbols: $\langle\sigma^2(t)\rangle$, the error bars are the rms variation of the time-averaged σ over the extent of the line. Solid line: prediction of Eq. (2) [27]; dashed line: Eq. (2) without the interaction term, $\frac{1}{9}\tilde{t}^3$. Dash-dotted line: prediction of Eq. (4). (c) Probability Density Functions (PDF) of ξ [Eq. (10)] at time delays $t = 15$, 30, and 50 μs ($\tilde{t} = 1.1$, 2.3, and 3.8, respectively).

B. Cloud dispersion at long times

To observe the widening of lines over long times (a few times τ_η) we have written single straight lines i in a strongly turbulent flow ($R_\lambda = 460$) and measured their average squared width $\langle\sigma_i^2(s,t)\rangle_i$, as a function of the delay time t between writing and reading. Averages $\langle\ \rangle_i$ were done over 4×10^3 lines, and over the extent of each individual line. Figure 5 shows the prediction of Eq. (2) [27], while the result of Eq. (4) is also compared to the experimental result. For short delay times Eq. (2) disagrees with the experiment, consistent with the result in Fig. 4. For longer delay times both the model Eqs. (4) and (2) are in fair agreement with the experiment, an agreement which owes to the $\propto \tilde{t}^3$ interaction term. Thus, this experiment demonstrates the interaction between molecular diffusion and turbulent dispersion.

The average line widening is but one aspect of turbulent dispersion. The stretching and squeezing of lines is caused by local gradients of the turbulent flow. In strong turbulence, the statistical properties of these gradients are highly non-Gaussian, with (stretched) exponential tails of the PDF; this should be inherited by the instantaneous line widths σ. Figure 5(c) shows the PDF of the scaled (squared) width ξ defined as

$$\xi = \frac{\sigma^2(\tilde{t}) - \langle\sigma^2(0)\rangle}{2\,\tilde{t}\,\langle\sigma^2(0)\rangle} - \frac{2}{\mathrm{Sc}\,\langle\widetilde{\sigma}^2(0)\rangle}\left(1 + \frac{1}{9}\tilde{t}^2\right), \tag{10}$$

at times $\tilde{t} = 1.1$, 2.3, and 3.8. According to Eq. (4), the average of ξ is the dimensionless strain rate S, suggesting that the fluctuations of ξ reflect the fluctuations of the strain rate. The PDF of the linewidths in Fig. 5(c) has long tails, which approximately scale with delay time t, such that the

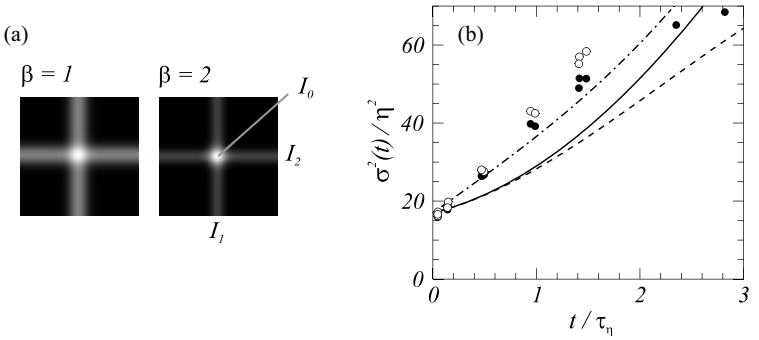

FIG. 6. The widening of dots in a turbulent flow. The dots are small molecular clouds that were created at the intersection of two laser beams, using the nonlinearity of NO formation. (a) Influence of the nonlinearity of the writing process. The intensities of the crossing lines are I_1 and I_2, while I_0 is the intensity of the intersection point. In the case of quadratic nonlinearity ($\beta = 2$), $I_0 = 2(I_1 + I_2)$. (b) Open circles: $\langle\sigma^2(t)\rangle$; the closed dots show the influence of the deformation of the cross due to turbulence, $\langle\sigma^2(t)\,\sin^2(\alpha_2 - \alpha_1)\rangle$. The statistical uncertainty is smaller than the symbol size. Full line: prediction of Eq. (2) [27]; dashed line: Eq. (2) without the interaction term $\frac{1}{9}\tilde{t}^3$. Dash-dotted line: prediction of Eq. (4).

fluctuations of ξ are approximately independent of delay time. This indeed suggests a link with the statistics of the strain rate.

C. Dispersion of 3D blobs

The creation of the NO tracer molecules through irradiation by an intense UV laser is a nonlinear process, and we have previously shown that the tagged NO molecule concentration depends quadratically on the laser intensity. This offers the opportunity to write three-dimensional blobs in the perpendicular intersection region of two laser beams [6].

Assuming Gaussian beam profiles with Gaussian widths σ, the concentration profile of a blob is

$$C(x, y) = C_0[e^{-x^2/\sigma^2} + e^{-y^2/\sigma^2}]^\beta, \tag{11}$$

where the intersection is assumed to be in the origin, and where $\beta = 1$ in the case that the written concentrations may simply be added and $\beta = 2$ for a writing process with quadratic nonlinearity. These two cases are illustrated in Fig. 6. In the case $\beta = 2$, the NO concentration profile has the shape of a cross with a highlighted center which is approximately Gaussian.

At initial time, the tagged NO lines cross at right angles, but at later times these lines will rotate, and we fit the intensity profile

$$I(x, y) = I_0\left[e^{-(y\cos\alpha_1 - x\sin\alpha_1)^2/\sigma^2} + e^{-(y\cos\alpha_2 - x\sin\alpha_2)^2/\sigma^2}\right]^2, \tag{12}$$

where α_1 is the angle of the initial horizontal line with the x axis, and α_2 is the angle of the initial vertical line with the x axis; at $t = 0$, $\alpha_1 = 0$ and $\alpha_2 = \pi/2$. In the analysis of the NO fluorescence images, the lines and their intersections were found using the technique of active contours, after which the function $I(x, y)$ was fitted to the intersection region, with the parameters I_0, σ, α_1, and α_2 determined in a least squares procedure. The intensity profile Eq. (12) is not a simple Gaussian. Due to the nonlinearity, the fitted σ over-estimates the true width. In addition, the apparent width changes due the deformation of the cross, such that $\alpha_2 - \alpha_1 \neq \pi/2$.

The initial concentration profile will disperse as time progresses, both its scale σ and its profile $C(x, y)$ will change. For $\beta = 2$, the cross term in Eq. (11) remains a solution of the diffusion equation. Therefore, we assume that σ remains appropriate for the change of scale.

Our laser beams are a mere 50 μm wide, and crossing them exactly in space is a challenge. The degree of spatial overlap can be monitored by a measurement of the fluorescence intensity I_0 in the

intersection point, compared to $I_{1,2}$ of the crossing lines (see Fig. 6). In the case of perfect overlap and quadratic nonlinearity, the quantity $I_0/(I_1+I_2) = 2^{\beta-1}$ (in case that $I_1 = I_2$). In our case we find a fair degree of overlap with an average ratio $I_0/(I_1+I_2) = 1.5 \pm 0.4$, where the error is the root-mean-square (rms) fluctuation.

The result of σ as a function of delay time is shown in Fig. 6, together with the predictions of Eqs. (2) and (4). Identifying crosses and fitting them is challenging, and the fate of these blobs could only be followed over limited time ($\widetilde{t} \lesssim 3$). The results agree with those for the spreading of lines. The discrepancy with the model Eq. (2) at small times is again evident, while both models highlight the importance of the interaction contribution.

D. Turbulent dispersion at inertial-range scales

A surprising consequence of the interaction of molecular diffusion with turbulence is that the center of mass of molecular clouds lags behind the dispersion of fluid parcels (while the growth of their size is enhanced) [13].

Two points $\boldsymbol{x}_1, \boldsymbol{x}_2$, which are separated by a distance Δ which lies in the inertial range will for short times separate ballistically; $\boldsymbol{x}_{1,2}(t) = \boldsymbol{x}_{1,2}(0) + \boldsymbol{u}_{1,2}\, t$, where the fluid velocities $\boldsymbol{u}_{1,2}$ are taken at their initial positions $\boldsymbol{x}_{1,2}(0)$ and $t = 0$. The fluctuation of their separation $\Delta(t)$ is then given by the statistics of the velocity difference $\boldsymbol{u}_2 - \boldsymbol{u}_1$ across Δ, that is, by the second-order velocity structure function. This is expressed by the well-known Batchelor formula [30],

$$\langle \Delta^2(t) \rangle - \Delta_0^2 = \frac{11}{3}\, C_2\, (\epsilon \Delta_0)^{2/3} t^2, \tag{13}$$

where $C_2 = 2.1$ is the universal constant of the inertial-range scaling law of the second-order longitudinal Eulerian structure function [40], $\langle [(\boldsymbol{u}_2 - \boldsymbol{u}_1) \cdot \boldsymbol{\Delta}(0)/\Delta(0)]^2 \rangle = C_2 \epsilon^{2/3}\, \Delta(0)^{2/3}$. and the factor $11/3$ owes to the isotropy of the velocity field. The question is until which delay time t the result Eq. (13) holds, and whether this result also applies to physical clouds, rather than mathematical points. Surprisingly, it was recently found experimentally that Eq. (13) holds to times $t/\tau_\eta \approx 30$, that is until after many small-eddy turnover times, when the assumption of linear-in-time displacement has become highly questionable [41].

In our experiment we write a double cross, with $\Delta(t)$ the separation of its nodes [see Fig. 6(a)]. These nodes are the intersection points of the centroids of the lines that make the double cross. Before discussing the separations Δ we show in Figs. 7(c)–7(f) the mean and rms positions of the left and right intersection points, $\langle x \rangle$, $\langle y \rangle$, and $\langle (x - \langle x \rangle)^2 \rangle^{1/2}$, $\langle (y - \langle y \rangle)^2 \rangle^{1/2}$, respectively. Both mean and rms positions increase linearly with time, defining mean U, V and turbulent u, v velocities. The mean velocities are $(U, V) = (1.6, 35.6)$ m/s and $(1.1, 37.2)$ m/s for the left and right dots, respectively, corresponding to the vertical orientation of the jet. The turbulent velocities, $(u, v) =$ $(7.8, 9.2)$ m/s and $(7.6, 9.2)$ m/s indicate a slight anisotropy of the flow.

In homogeneous and isotropic turbulence with zero mean flow, the mean separation $\langle \boldsymbol{\Delta}_i(t) \rangle_i$ would be constant and equal to $\boldsymbol{\Delta_0}$. To correct for the slight inhomogeneity and anisotropy in our flow, we define the initial separation at each time delay t as the mean $\boldsymbol{\Delta}_0 = \langle \boldsymbol{\Delta}_i(t) \rangle_i$.[3] Writing a double cross and registering it a time t later is repeated 4×10^3 times at each t. From these images we collect the statistics of $\boldsymbol{\Delta}(t) = \boldsymbol{x}_2 - \boldsymbol{x}_1$. The results are shown in Fig. 6(c), and compared with Batchelor's prediction Eq. (13). Because we measure $\Delta(t)$ in a two-dimensional projection of the actual separation, the isotropy factor $11/3$ in Eq. (13) now becomes $7/3$. We emphasize that the computation of Batchelor's prediction does not involve adjustable parameters; the dissipation rate ϵ was measured in a separate experiment. The statistical error of $\langle \Delta^2(t) \rangle - \Delta_0^2$ is smaller than

[3]This makes the left-hand side of Eq. (13) equivalent to that used in Ref. [41], which involves the difference $\langle |\boldsymbol{\Delta}(t) - \boldsymbol{\Delta}_0|^2 \rangle$. Interestingly, in Ref. [42] the authors of Ref. [41] find that the proper Eq. (13) does not agree with their data.

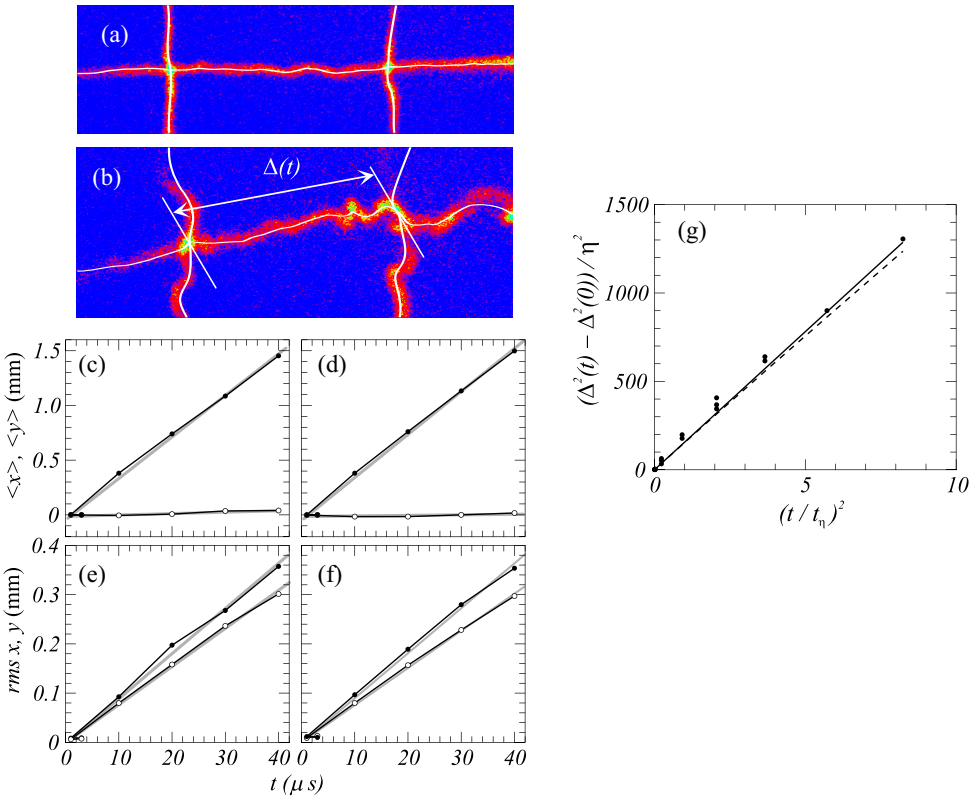

FIG. 7. The dispersion of two dots in turbulence that at $t = 0$ have an inertial-range separation $\Delta(0) = 200\,\eta$. The separation $\Delta(t)$ is defined as the distance between the intersection points of three lines written in a turbulent flow. (a) Image of double cross, $t = 10$ μs after it was written, (b) delay time of $t = 40$ μs. (c, d) Mean displacement of the left and right intersection point, dots: $\langle y\rangle$, open circles: $\langle x\rangle$. The corresponding mean velocities are $(U, V) = (1.6, 35.6)$ m/s and $(1.1, 37.2)$ for the left and right dots, respectively. (e, f) Root-mean-square displacement, dots: $\langle(y - \langle y\rangle)^2\rangle^{1/2}$, open circles: $\langle(x - \langle x\rangle)^2\rangle^{1/2}$. The corresponding turbulent velocities are $(u, v) = (7.8, 9.2)$ m/s and $(7.6, 9.2)$ for the left and right dots, respectively. Mean and rms velocities were found from linear fits [gray lines in panels (c–f)]. (g) Dots: measured $\langle\Delta^2(t)\rangle - \Delta^2(0)$ as function of delay time t. Line: prediction of the Batchelor formula, dashed line: Batchelor formula including interaction of diffusion with turbulence.

the size of the dots in Fig. 6. What remains are systematic errors due to pointing stability of the laser beams.

The excellent agreement of Batchelor's formula Eq. (13) with the experiment is remarkable because the measured $\Delta(t)$ is the separation between the centroids of big molecular clouds whose size grows to $\approx 10\,\eta$ at the longest delay time. This growth is mainly due to the churning of small-scale eddies. Clearly, our results demonstrate that this small-scale growth and the large-scale dispersion are independent.

The interaction with molecular diffusion causes the centroids of the molecular clouds to lag behind the fluid parcels that carry them. In dimensionless units, the squared distance lags by $4\tilde{t}^3/3$ Sc [13]. As the largest time in our experiment is $\tilde{t} \approx 3$, and the largest distance is $\widetilde{\Delta}^2 \approx 10^3$, this effect is smaller than the accuracy of our experiment.

The largest time delay in our experiment is 60 μs $\approx 3\,\tau_\eta$. At times $t > (\Delta_0^2/\epsilon)^{1/3}$ [dimensionless $\tilde{t} > \widetilde{\Delta}_0^{2/3}$], the large eddy with size Δ_0 that contains the two intersection points breaks up and

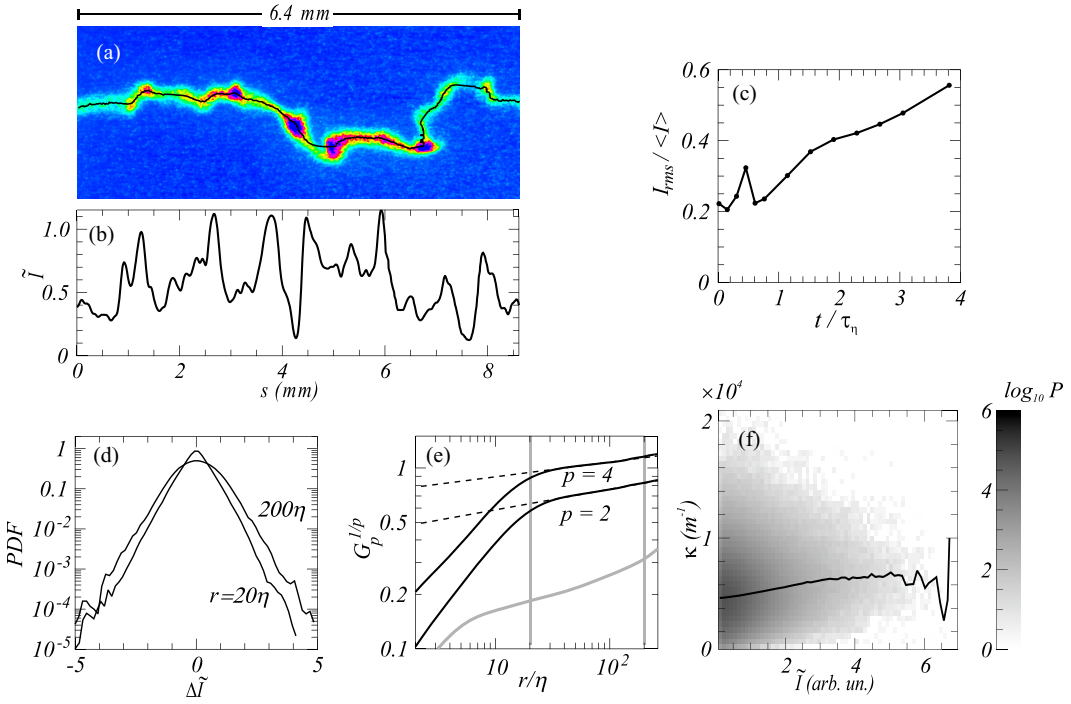

FIG. 8. (a) Image of a line of NO molecules for delay time $t = 30$ μs (2.3 τ_η). The black line traces its backbone $\boldsymbol{x}(s)$. (b) Normalized line intensity $\widetilde{I}(s)$ as a function of the curvilinear coordinate s along the line (the length of this line is larger than the 6.4 mm width of the image). The intensity $\widetilde{I}(s)$ has been filtered using a binomial filter with width 2 η. (c) Rms intensity fluctuation along lines as a function of delay time between writing and reading. (d) PDF of increment $\delta\widetilde{I}(r)$ for separations $r = 20\,\eta$ and 200 η and delay time $t = 50$ μs (3.8 τ_η). (e) Structure functions $G_p^{1/p}(r) = \langle(\widetilde{I}_i(s+r) - \widetilde{I}_i(s))^p\rangle_{i,s}^{1/p}$ for orders $p = 2, 4$ and delay time $t = 50$ μs. Dashed lines: fits of inertial range behavior $G_p(r) \sim r^{\zeta_p}$, with $\zeta_p \approx 0.1\,p$. Gray line: $G_2^{1/2}$ of lines at $t = 2$ μs, which provides an estimate of the uncertainty of the results at $t = 50$ μs. (f) Joint histogram $P(\kappa, I)$ of curvature κ and intensity I, line: mean $\langle\kappa\rangle$ as a function of intensity I. Curvatures were computed over intervals $l_c = 15\,\eta$. The shades of gray are on a logarithmic scale. The correction for the intensity variation of writing and reading lasers over the image plane was discussed in Sec. III B.

the separation is predicted to follow Richardson's statistics, $\langle\Delta^2(t)\rangle = g\,\epsilon\,t^3$, with g the universal Richardson constant [34,43]. If we take $\widetilde{\Delta}_0 = 30$ as the smallest separation inside the inertial range, then $\tilde{t} > 10$. Even for the smallest length scale in our experiments, $\widetilde{\Delta}_0 \approx 4$, $\tilde{t} > 2.5$ before Richardson scaling can be observed. Therefore, the Richardson regime is inaccessible in this experiment.

E. Concentration fluctuations

Well-mixed tracers in an incompressible homogeneous turbulent flow remain well-mixed. This is not so for a subset of tracers that are tagged at initial time in a specific region, such as the written lines in our experiment. Lines are stretched and wrinkled by turbulence and tracers along the line are redistributed, leading to lumps and even rupture. This is illustrated in Fig. 8 where we show a wrinkled line together with the intensity $I(s)$ on the line backbone $\boldsymbol{x}(s)$. Throughout we assume that the intensity $I(s)$ is proportional to the NO tracer concentration. The question is now about the statistical properties of $I(s)$.

It is well known that an unmixed tracer distribution $C(\boldsymbol{r})$ in a turbulent flow develops large concentration fluctuations at small scales. These fluctuations are characterized by the Eulerian structure functions of order p, $G_p(r\hat{\boldsymbol{e}}) = \langle [C(\boldsymbol{x} + r\,\hat{\boldsymbol{e}}) - C(\boldsymbol{x})]^p \rangle_{\boldsymbol{x}}$. In the inertial range $G_p(r)$ has scaling behavior, $G_p(r) \sim r^{\zeta_p}$, which does not depend on the direction vector $\hat{\boldsymbol{e}}$ in isotropic scalar turbulence. The traditional view has been that the value of the scaling exponent ζ_p is inherited from a self-similar velocity field, $\zeta_p = p/3$: the Kolmogorov-Obukhov-Corrsin theory [44]. However, it was found recently both in experiments and direct numerical simulations that ζ_p is strongly anomalous, that is, it is much less than $p/3$, and actually could reach an asymptote for large p [45]. In addition, the return to isotropy at small scales (small r) is marred by the emergence of ramp-cliff structures which are inherited from the imposed large-scale concentration gradients [46–49].

The statistical properties of the intensity variation along the line, $\widetilde{I}(s)$ can be quantified using the increments $\Delta\widetilde{I}_i = \widetilde{I}_i(s+r) - \widetilde{I}_i(s)$, with moments $\langle (\Delta\widetilde{I}_i)^p \rangle_{s,i}$, and averages $\langle \cdots \rangle_{s,i}$ over the curvilinear coordinate s and lines i. These moments can be compared to the concentration structure function $G_p(r)$, with r an increment of the curvilinear coordinate. Note that this concentration structure function differs both from the Eulerian and Lagrangian ones, it describes the spatial increments along a deforming Lagrangian object. Similar mixed Eulerian–Lagrangian structure functions have been discussed by Calzavarini *et al.* [50].

Probability density functions $P(\Delta\widetilde{I})$ at separations $r = 20\,\eta$ and $200\,\eta$ are shown in Fig. 8(d). The PDF's are non-Gaussian, but contrary to the PDF's of the velocity increments (see Sec. V), the shape does not vary strongly across the inertial range. Structure functions $G_p^{1/p}$ of order $p = 2, 4$ are shown in Fig. 8(e). They exhibit a clear inertial-range ($r \gtrsim 20\,\eta$) scaling behavior, $G_p(r) \sim r^{\zeta_p}$, but with a scaling exponent $\zeta_2 \approx 0.2$ which is completely different from the Kolmogorov one, $\zeta_2 = 2/3$. Moreover, the scaling exponents are self-similar, $\zeta_p \approx 0.1\,p$, which, again, is very different from self-similar turbulence, $\zeta_p = p/3$. Scaling exponents of *Lagrangian* scalar concentration structure functions, $G_p(\tau) = \langle [C(\boldsymbol{x}(t+\tau)) - C(\boldsymbol{x}(t))]^p \rangle$, have been studied numerically by Bec *et al.* [51]. Their self-similar form would be $G_p(\tau) \sim \tau^{p/2}$.

Registered lines suffer from photon collection noise, leading to noise in $\widetilde{I}_i(s)$. The effect on structure functions can be estimated from lines measured at short delay times that are unaffected by turbulence; these results are also shown in Fig. 8(e), and demonstrate the significance of our conclusions.

The fluctuating intensity on the line—a Lagrangian object—is clearly outside the context of the Kolmogorov-Obukhov-Corrsin phenomenology [44]. Inspection of Fig. 8(a) suggests a relation between the concentration maxima and the curvature of the line backbone. The folding and stretching of material lines in numerical turbulence was recently discussed by Bentkamp *et al.* [52]. They observed a stationary, algebraic PDF of local curvatures, even after a short time ($4.16\,\tau_\eta$).

We measured line curvatures $\kappa(s_0)$ at $\boldsymbol{x}(s_0)$ by fitting quadratic polynomials to $x(s)$ and $y(s)$ over intervals $[s_0 - l_c/2, s_0 + l_c/2]$, from which $\kappa(s_0) = [x''^2(s_0) + y''^2(s_0)]^{1/2}$ was determined. The smaller l_c, the larger curvature can be detected. For material lines there is no lower limit on l_c. In Ref. [52] curvature radii as small as $10^{-7}\,\eta$ are found.[4] For the physical lines in our experiment, l_c is bounded by diffusion, and thus by σ. Smaller l_c than 8η gives larger curvature, but it is determined by photon noise.

The joint PDF of curvature κ and intensity I and the dependence of the average κ on intensity in Fig. 8(d) indeed suggest a weak correlation between the average curvature and intensity I.

V. VELOCIMETRY

Velocimetry can be done by registering the displacements of lines, however, it is not unambiguous. Crudely, the vertical displacement $\Delta y(x)$ of a point x on the line in a time t gives the vertical

[4] If lines in Ref. [52] were physical instead of mathematical, then the required Schmidt number, which follows from $l_c \approx (4\mathrm{Sc}^{-1} t/\tau_\eta)^{1/2}\,\eta$, would have been $\mathrm{Sc} \approx 10^{12}$, which is unphysical.

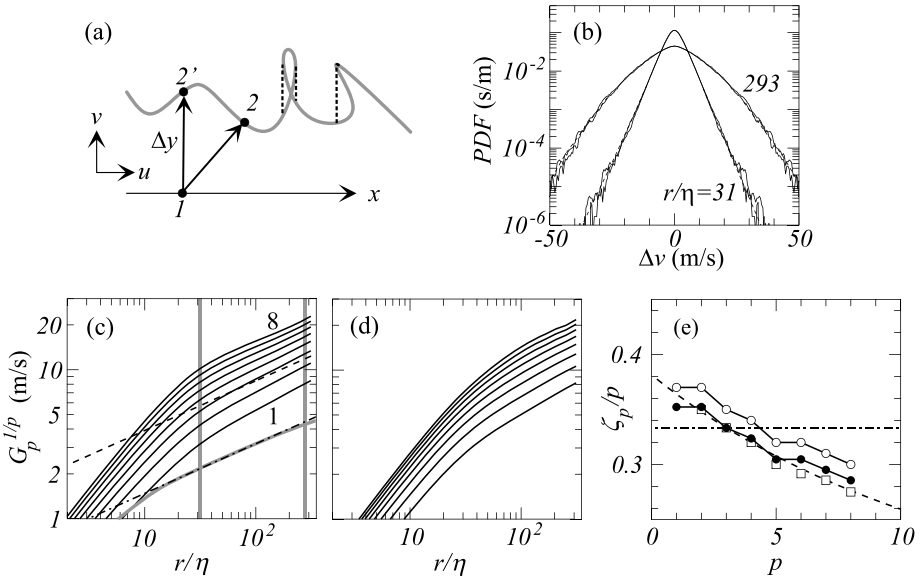

FIG. 9. Velocimetry of turbulent flows from the deformation of lines that is visualized a time t after writing. (a) We infer the v component of the velocity from the perpendicular displacement Δy of the point $1 \to 2'$, $v = \Delta y/t$, while the true Lagrangian displacement is $1 \to 2$. Overhangs and self-intersections in the two-dimensional projection are replaced by their convex hull (dashed lines). (b) Full lines: probability density functions $P[\Delta v(r)]$ of transverse velocity increments at $r/\eta = 31$, and $r/\eta = 293$, respectively [indicated by the gray lines in panel (c)]. Dashed lines (mostly hidden by the full lines): fits of stretched exponential to the tails of the PDF's, $P(\Delta v) = a\ \exp(-\alpha|\Delta v|^{\beta})$. Velocities are from line displacements after a delay time $t = 10$ μs. To illustrate the symmetry of the PDF's, $P(\Delta v)$ and $P(-\Delta v)$ are shown overlayed. (c) Structure functions with $p = 1, \ldots, 8$ measured from line displacements at a delay $t = 10$ μs. The structure functions have been raised to the power $1/p$; in a self-similar picture they would show inertial-range ($r \gtrsim 30\ \eta$) algebraic behavior, $G_p^{1/p}(r) \sim r^{\zeta(p)/p}$ with the same slope $\zeta(p)/p = 1/3$. Dashed line: Kolmogorov prediction $G_2 = \frac{4}{3}C_2\epsilon^{2/3}r^{2/3}$. Gray line: hot-wire measurement at $R_\lambda = 200$, dash-dot line: Kolmogorov prediction. (d) Same as panel (c), but now for a time delay $t = 30$ μs. (e) Open circles: scaling $\zeta(p)/p$ exponents determined from structure functions summed over 2 time delays ($t = 6$, and 8 μs). Closed dots, same $\zeta(p)/p$ but now normalized such that $\zeta(3) = 1$. Open squares (partly obscured by closed dots): results of Noullez *et al.*, which were determined from plots of $\log G_p$ versus $\log G_3$ [12]. Dash-dotted line: Kolmogorov's self-similar prediction [16], dashed line: log-Poisson model [54].

component of the velocity $v(x) = \Delta y/t$. The situation is sketched in Fig. 9(a). The problem is the error made when translating Lagrangian line displacements into Eulerian velocities. Errors arise from ignoring the horizontal u-velocity component of a point on a written line, and from the 2D projection of the deformed line which may even result in apparent self-intersections. In the analysis of our results, these loops are replaced by their convex hull [see Fig. 9(a)]. The same procedure was applied to line overhangs. These errors aggravate for longer time delays t.

From the velocities $v(x)$ we can form the increments $\Delta v(r) = v(x + r) - v(x)$, their probability density function $P[\Delta v(r)]$ and its moments. Structure functions quantify the statistical properties of the velocity difference $\Delta v(r)$ measured across a distance r. In isotropic turbulence there are two distinct ways to define this velocity increment. In the longitudinal case, the velocity component points in the same direction as the separation vector $\boldsymbol{r}$ while in the transverse case they are perpendicular. In our experiments we infer the *transverse* structure functions $G_p(r)$ from line displacements in the y direction:

$$G_p(r) = \langle[\Delta v^p(r)]\rangle = \langle[v(x + r) - v(x)]^p\rangle,$$

which can be phrased in terms of the probability density functions (PDF) $P_r(\Delta v)$,

$$G_p(r) = \int_{-\infty}^{\infty} P_r(\Delta v)\,(\Delta v)^p d(\Delta v).$$

As we write and observe single lines with a repetition rate which is set by the pulse rate of the laser (10 Hz), our lines are completely independent and longitudinal velocity increments can not be determined.[5]

Figure 9(b) shows probability density functions $P[\Delta v(r)]$ measured for two different separations, $r/\eta = 31$ and $r/\eta = 293$, respectively. The velocity increments inferred from line displacements were accumulated for 4×10^3 lines and delay time $t = 10\,\mu s$ ($\tilde{t} = t/\tau_\eta = 0.8$). Contrary to the longitudinal case, the statistics of transverse velocity increments should be perfectly symmetric, $P(\Delta v) = P(-\Delta v)$ in homogeneous turbulence. This is demonstrated by overlaying $P[\Delta v(r)]$ and $P[-\Delta v(r)]$ in Fig. 9(b). For large separations r the probability density functions tend to Gaussian since the velocities at $x + r$ and x become increasingly decorrelated, while for small separations their large Δv tails are compatible with stretched exponentials, $P_r(\Delta v) = a\, e^{-\alpha|\Delta v|^\beta}$, with $\beta < 1$. A fit of these stretched exponentials is also shown in Fig. 9(b). The change of β from $\beta < 1$ at small separations r to $\beta = 2$ for the Gaussian case at large r is characteristic of intermittency and leads to a nontrivial dependence of the scaling exponents ζ_p of the structure functions on the order p.

We note, as also do Noullez *et al.* [12], that very large velocity differences are observed over very short distances: they have been found as large as $30\,m\,s^{-1}$ over a mere $400\,\mu m$. This must be compared to the mean velocity $V = 45\,m\,s^{-1}$ and rms velocity $v = 12\,m\,s^{-1}$.

To illustrate our argument that MTV in a gas cannot resolve motion on the smallest scale, we note that for the data of Fig. 9 the initial line width is $\tilde{\sigma}(0) = 3.7$, which doubles after a delay of $\tilde{t} = 0.7$ ($t = 10\,\mu s$). Even when $\tilde{\sigma}(0) = 1$ (the Kolmogorov length), it would have increased by a factor 2.5 after $\tilde{t} = 1$ (the Kolmogorov time).

To study the influence of the time delay t on high-order structure functions, we plot in Figs. 9(c) and 9(d) transverse structure functions of orders 1 to 8 in a log-log plot for $t = 10\,\mu s = 0.8\,\tau_\eta$ and $t = 30\,\mu s = 2.3\,\tau_\eta$. Their deviation from self-similarity is illustrated by plotting $G_p^{1/p}(r)$. If Kolmogorov's (1941) self-similar turbulence description would hold, then structure functions would scale algebraically with the same exponent $G_p^{1/p}(r) \sim r^{1/3}$ [16].

While at $t = 10\,\mu s$ a clear inertial range can be observed, it is virtually absent at $t = 30\,\mu s$ due to the large line deformations. A compromise must be sought as to the delay time used. Shorter delay times lead to less accurate velocities, but also to less severe line deformations. The Kolmogorov prediction for the second-order structure function is $G_2(r) = \frac{4}{3}\, C_2\, \epsilon^{2/3}\, r^{2/3}$, with the Kolmogorov constant $C_2 = 2.1$ [40], and where the factor $4/3$ emerges because of the transverse arrangement; see Fig. 9(c). The measured G_2 has a larger scaling exponent, and under-estimates the dissipation rate ϵ. Indeed, its estimate from G_2 at the smallest separation r', $\epsilon = \frac{15}{2}\, \nu\, G_2(r')/r'^2 = 7.7 \times 10^4\ m^2 s^{-3}$ is smaller than the estimate from Eq. (7), $\epsilon = 9.1 \times 10^4\ m^2 s^{-3}$. Hot-wire experiments were used to calibrate the setup at lower Reynolds numbers. A transverse structure function from these measurements is shown in Fig. 9(c); it perfectly agrees with the Kolmogorov prediction.

We have determined the exponents ζ_p from velocity structure functions summed over time delays $t = 6$, and 8 μs, corresponding to 8×10^3 lines, with 1024 velocity increments each. However, it is not enough to determine the high orders sufficiently accurately. Because of the symmetry of the PDF of transverse velocity increments, the odd moments $p = 1, 3, \ldots$ vanish and we define all moments in terms of absolute values $|\Delta v|$.

The exponents ζ_p are shown in Fig. 9(e). After normalizing them, such that $\zeta_3 = 1$, ζ_p follows the prediction of the log-Poisson model [54] which appears to correctly parametrize most experimental

[5]Experiments on anisotropic turbulence involving more general structure functions were discussed by Cekli and van de Water [53].

results. Our normalized results agree with those of Noullez *et al.* which are also shown in Fig. 9(e) [12]. Much as theirs, the present results are nonintrusive measurements of transverse structure functions, while the other experiments use hot-wire probes, mostly in the arrangement which necessitates invocation of Taylor's frozen turbulence hypothesis.

Noullez *et al.* [12] were the first to measure high-order transverse structure functions using molecular tagging. Although our normalized results agree, there are differences. Contrary to that of Ref. [12] our exponent ζ_3 is significantly larger than 1. It appears that this anomaly increases with increasing delay time. The scaling exponents in Fig. 9(c) were determined directly, whereas Ref. [12] found them by plotting structure functions $G_p(r)$ as a function of $G_3(r)$ [55]. Finally, the molecular tracers in Ref. [12] are oxygen molecules excited to fragile metastable vibrational states, with a lifetime limited to $\approx$10 μs by collisions with water molecules. Our results do not support a stronger anomaly of the transverse scaling exponents compared to the longitudinal ones. It has been suggested that the transverse velocity increments are more intermittent than the longitudinal ones because of the greater ease to capture violent events in the transverse configuration [12]. However, here this issue remains undecided as the statistical accuracy of our experiments does not allow to reach large moments p.

VI. CONCLUSION

Molecular tagging in a turbulent gas can be used for velocimetry [12,56], but it fundamentally cannot resolve motion on the smallest scales due to the interaction with diffusion [6]. This severely limits its use as a tool for velocimetry. However, we have shown that it can retrieve the known anomalous scaling of transverse structure functions. However, tagging molecules opens up a unique view on small-scale turbulent mixing. This avenue has been followed in the present paper.

The structures that we write in a strongly turbulent flow probe the initial episode of turbulent mixing. It is characterized by the subtle interplay between molecular diffusion and turbulent strain: without diffusion two very close points would take an infinitely long time to separate to the Kolmogorov scale. Once the cloud becomes sizable, turbulent dispersion takes over. Specifically, in the presence of diffusion, a point with initial size $\widetilde{\sigma}(0) = 0$ will grow to $\widetilde{\sigma}^2 = 4$ in a time $\tilde{t} = 1$, but without diffusion it would take an initial size $\widetilde{\sigma}^2(0) = 2$ for a blob to grow to $\widetilde{\sigma}^2 = 4$ in the same time interval.

Before they are dispersed by the large-scale eddies, objects such as lines and clouds develop large concentration fluctuations. Structure functions show scaling behavior and an inertial range, but with scaling exponents that cannot be compared to the ones known from the fluctuations of the velocity field, or from the concentration fluctuations of dispersion driven by a large-scale gradient.

ACKNOWLEDGMENTS

We gratefully acknowledge financial support by the Dutch Research Council. We are grateful for the results of M. Pashtrapanska on the two-dot dispersion. We also thank M. Mirzaei for performing experiments. The helpful remarks of R. McMullen are greatly appreciated.

[1] R. B. Miles and W. R. Lempert, Quantitative flow visualization in unseeded flows, Annu. Rev. Fluid Mech. **29**, 285 (1997).

[2] M. M. Koochesfahani and D. G. Nocera, Molecular tagging velocimetry, in *Handbook of Experimental Fluid Dynamics*, edited by J. Foss, C. Tropea, and A. Yarin (Springer-Verlag, Berlin, 2007), Chap. 5.4.

[3] G. S. Diskin, W. R. Lempert, and R. B. Miles, Observation of vibrational relaxation dynamics in $x^3\sigma_g^-$ oxygen following stimulated Raman excitation to the $v = 1$ level: Implications for the RELIEF flow tagging technique, Report No. AIAA Paper 96-0301, NASA, 1996.

[4] N. J. Dam, R. J. H. Klein-Douwel, N. M. Sijtsema, and J. J. ter Meulen, Nitric oxide flow tagging in unseeded air, Opt. Lett. **26**, 36 (2001).
[5] N. J. DeLuca, R. B. Miles, N. Jiang, W. D. Kulatolaka, A. K. Patnaik, and J. R. Gord, FLEET velocimetry for combustion and flow diagnostics, Appl. Opt. **56**, 8632 (2017).
[6] J. Bominaar, T. Elenbaas, M. Pashtrapanska, N. Dam, J. J. ter Meulen, and W. van de Water, Writing in turbulent air, Phys. Rev. E **77**, 046312 (2008).
[7] F. Li, H. Zhang, and B. Bai, A review of molecular tagging technique, Measurement **171**, 108790 (2021).
[8] R. W. Pitz, J. A. Wehrmeyer, L. A. Ribarov, D. A. Oguss, F. Batliwala, P. A. D. S. Deusch, and P. E. Dimotakis, Unseeded molecular flow tagging in cold and hot flows using ozone and hydroxyl tagging velocimetry, Meas. Sci. Technol. **11**, 1259 (2000).
[9] R. Sánchez-González, R. Srinivasan, R. D. W. Bowersox, and S. W. North, Simultaneous velocity and temperature measurements in gaseous flow fields using the VENOM technique, Opt. Lett. **36**, 196 (2011).
[10] E. M. Thurlow and J. C. Klewicki, Experimental study of turbulent Poiseuille–Couette flow, Phys. Fluids **12**, 865 (2000).
[11] M. Mirzaei, N. J. Dam, and W. van de Water, Molecular tagging velocimetry in turbulence using biacetyl, Phys. Rev. E **86**, 046318 (2012).
[12] A. Noullez, G. Wallace, W. Lempert, R. B. Miles, and U. Frisch, Transverse velocity increments in turbulent flow using the RELIEF technique, J. Fluid Mech. **339**, 287 (1997).
[13] P. G. Saffman, On the effect of the molecular diffusivity in turbulent diffusion, J. Fluid Mech. **8**, 273 (1960).
[14] A. A. Townsend, The diffusion of heat spots in isotropic turbulence, Proc. R. Soc. London A **209**, 418 (1951).
[15] A. A. Townsend, The diffusion behind a line source in homogeneous turbulence, Proc. R. Soc. London A **224**, 487 (1954).
[16] U. Frisch, *Turbulence, The Legacy of A. N. Kolmogorov* (Cambridge University Press, New York, 1995).
[17] W. R. Mickelsen, Measurements on the effect of molecular diffusivity in turbulent diffusion, J. Fluid Mech. **7**, 397 (1960).
[18] A. Mazzino and M. Vergassola, Interference between turbulent and molecular diffusion, Europhys. Lett. **37**, 535 (1997).
[19] K. Kontomaris and T. J. Hanratty, Effect of molecular diffusivity on point source diffusion in the center of a numerically simulated turbulent channel flow, Int. J. Heat Mass Transf. **37**, 1817 (1994).
[20] P. C. Chatwin and P. J. Sullivan, The relative diffusion of a cloud of passive contaminant in incompressible turbulent flow, J. Fluid Mech. **91**, 337 (1979).
[21] G. I. Taylor, Diffusion of soluble matter in solvent flowing slowly through a tube, Proc. R. Soc. London A **219**, 186 (1953).
[22] P. B. Rhines and W. R. Young, How rapidly is a passive scalar mixed within closed streamlines? J. Fluid Mech. **133**, 133 (1983).
[23] G. I. Taylor, Diffusion by continuous movements, Proc. London Math. Soc. **S2-20**, 196 (1921).
[24] S. B. Pope, The vanishing effect of molecular diffusivity on turbulent dispersion: Implications for turbulent mixing and the scalar flux, J. Fluid Mech. **359**, 299 (1998).
[25] W. van de Water, N. Dam, and E. Calzavarini, Dispersion of molecular patterns written in turbulent air, Phys. Rev. Lett. **129**, 254501 (2022).
[26] B. L. Sawford and J. C. R. Hunt, Effects of turbulence structure, molecular diffusion and source size on scalar fluctuations in homogeneous turbulence, J. Fluid Mech. **165**, 373 (1986).
[27] D. Buaria, P. K. Yeung, and B. L. Sawford, A Lagrangian study of turbulent mixing: Forward and backward dispersion of molecular trajectories in isotropic turbulence, J. Fluid Mech. **799**, 352 (2016).
[28] D. Buaria, B. L. Sawford, and P. K. Yeung, Characteristics of backward and forward two-particle relative dispersion in turbulence at different Reynolds numbers, Phys. Fluids **27**, 105101 (2015).
[29] R. M. Kerr, Higher-order derivative correlations and the alignment of small-scale structures in isotropic numerical turbulence, J. Fluid Mech. **153**, 31 (1985).
[30] G. K. Batchelor, Diffusion in a field of homogeneous turbulence: II. The relative motion of particles, Proc. Cambridge Philos. Soc. **48**, 345 (1952).

[31] R. Dhariwal and A. D. Bragg, Fluid particles only separate exponentially in the dissipation range after extremely long times, Phys. Rev. Fluids **3**, 034604 (2018).
[32] D. Buaria, E. Bodenschatz, and A. Pumir, Vortex stretching and enstrophy production in high Reynolds number turbulence, Phys. Rev. Fluids **5**, 104602 (2020).
[33] G. K. Batchelor, The effect of homogeneous turbulence on material lines and surfaces, Proc. R. Soc. London A **213**, 349 (1952).
[34] L. F. Richardson, Atmospheric diffusion shown on a distance-neighbour graph, Proc. R. Soc. London A **110**, 709 (1926).
[35] B. R. Pearson, P.-A. Krogstad, and W. van de Water, Measurements of the turbulent energy dissipation rate, Phys. Fluids **14**, 1288 (2002).
[36] W. van de Water and N. Dam, How to find patterns written in turbulent air, Exp. Fluids **54**, 1574 (2013).
[37] M. Kass, A. Witkin, and D. Terzopoulos, Snakes: Active contour models, Int. J. Comput. Vision **1**, 321 (1988).
[38] C. Xu and J. L. Prince, Snakes, shapes and gradient vector flow, IEEE Trans. Image Process. **7**, 359 (1998).
[39] W. J. Massman, A review of the molecular diffusivities of H_2O, CO_2, CH_4, CO, O_3, SO_2, NH_3, N_2O, NO, in air, O_2 and N_2 near STP, Atmos. Environ. **32**, 1111 (1998).
[40] P. K. Yeung and Y. Zhou, Universality of the Kolmogorov constant in numerical simulations of turbulence, Phys. Rev. E **56**, 1746 (1997).
[41] M. Bourgoin, N. T. Ouelette, H. Xu, J. Berg, and E. Bodenschatz, The role of turbulent pair dispersion in turbulent flow, Science **311**, 835 (2006).
[42] N. T. Ouellette, H. Xu, M. Bourgouin, and E. Bodenschatz, An experimental study of turbulent relative dispersion models, New J. Phys. **8**, 109 (2006).
[43] B. Sawford, Turbulent relative dispersion, Annu. Rev. Fluid Mech. **33**, 289 (2001).
[44] A. S. Monin and A. M. Yaglom, *Statistical Fluid Mechanics* (MIT Press, Cambridge, MA, 1975).
[45] A. Celani, A. Lanotte, A. Mazzino, and M. Vergassola, Fronts in passive scalar turbulence, Phys. Fluids **13**, 1768 (2001).
[46] M. Holzer and E. D. Siggia, Turbulent mixing of a passive scalar, Phys. Fluids **6**, 1820 (1994).
[47] C. Tong and Z. Warhaft, On passive derivative statistics in grid turbulence, Phys. Fluids **6**, 2165 (1994).
[48] K. P. Iyer, J. Schumacher, K. R. Sreenivasan, and P. K. Yeung, Steep cliffs and saturated exponents in three-dimensional turbulence, Phys. Rev. Lett. **121**, 264501 (2018).
[49] D. Buaria, M. P. Clay, K. R. Sreenivasan, and P. K. Yeung, Small-scale anisotropy and ramp-cliff structures in scalar turbulence, Phys. Rev. Lett. **126**, 034504 (2021).
[50] E. Calzavarini, Y. X. Huang, F. G. Schmitt, and L. P. Wang, Popelled microprobes in turbulence, Phys. Rev. Fluids **3**, 054604 (2018).
[51] J. Bec, H. Homann, and G. Krstulovic, Clustering, fronts, and heat transfer in turbulent suspensions of heavy particles, Phys. Rev. Lett. **112**, 234503 (2014).
[52] L. Bentkamp, T. D. Drivas, C. C. Lalescu, and M. Wilczek, The statistical geometry of material loops in turbulence, Nat. Commun. **13**, 2088 (2022).
[53] H. E. Cekli and W. van de Water, Stirring anisotropic turbulence with an active grid, Phys. Fluids **32**, 075119 (2020).
[54] Z.-S. She and E. Leveque, Universal scaling laws in fully developed turbulence, Phys. Rev. Lett. **72**, 336 (1994).
[55] R. Benzi, S. Ciliberto, R. Tripiccione, C. Baudet, F. Massaioli, and S. Succi, Extended self-similarity in turbulent flows, Phys. Rev. E **48**, R29(R) (1993).
[56] B. Stier and M. M. Koochesfahani, Molecular tagging velocimetry (MTV) measurements in gas phase flows, Exp. Fluids **26**, 297 (1999).